Can we use X-ray CT to generate 3D penetration resistance data?

Maxime Phalempin [a,*], Ulla Rosskopf [b], Steffen Schlüter [a], Doris Vetterlein [a,c], Stephan Peth [b]

[a] Department of Soil System Science, Helmholtz Centre for Environmental Research – UFZ, Theodor-Lieser-Strasse. 4, 06120 Halle/Saale, Germany
[b] Institue of Soil Science, Leibniz University Hannover, Herrenhäuser Straße 2, 30419 Hannover
[c] Soil Science, Martin-Luther-University Halle-Wittenberg, Von-Seckendorff-Platz 3, 06120 Halle/Saale, Germany

ARTICLE INFO

ABSTRACT

Noninvasive imaging of soils with X-ray CT has proven to be a useful method to assess soil structure from a pore space perspective. In contrast, methods like cone penetration tests reflect soil structure from the perspective of the soil matrix as assessed by its mechanical strength. Because both the gray value (GV) obtained with X-ray CT and the penetration resistance (PR) obtained with a cone penetration test depend on soil density there should be a relationship between the two. To the best of our knowledge, no studies attempted so far to investigate the nature of the PR ~ GV relationship and to understand how well PR and GV are correlated. We aimed at bridging that gap and carried out a combined analysis of local GV and PR with undisturbed soil cores sampled in two soil textures, *i.e.*, loam and sand. To carry out the GV measurements, we developed a new approach which considers an adaptive volume of the zone of influence of the penetrometer tip as a function of soil density. For sand and when looking at samples individually, the correlation between PR and GV was best when the soil microscale heterogeneity was high, *i.e.*, when dense and loose zones of soil were present on the course of the penetrometer tip. For loam, the correlation between PR and GV was not dependent on soil heterogeneity. When looking at the whole dataset, the agreement between PR and GV was better in loam than in sand, with a distance correlation metric of 0.66 for loam and 0.34 for sand, respectively. For loam, the relationship PR ~ GV had a trend which was similar to that of a hyperbola, *i.e.*, with escalating PR values in a narrow GV range. For sand, no particular model could be recognized. In order to provide a proof-of-concept on how to generate 3D PR maps, the co-located measurements of GV and PR were used to establish an empirical relationship and X-ray CT was used to extrapolate it in 3D. This was carried out with the loam dataset by fitting a hyperbolic function to the PR ~ GV data pairs. This model was then used to convert GVs into PR values, at a spatial resolution equal to that of the shaft diameter of the penetrometer tip we have used. Notwithstanding the fact that the suggested approach is dependent on numerous experimental conditions and edaphic factors, we advocate for the use of 3D PR maps. These maps could be used in root-soil interactions research, for which the study and breeding of cultivars that could show plastic response in their root systems under mechanical stress is becoming more and more important. This is particularly relevant in the context of mechanized modern agriculture.

1. Introduction

Soil penetration resistance (PR), also referred to as "mechanical impedance" or "strength", is a soil property which is commonly measured in geotechnical surveys (Lunne et al., 2002) as well as for the assessment of agronomic measures such as tillage operations (Bauder et al., 1981; Grant & Lafond, 1993; Lampurlanés and Cantero-Martínez, 2003) and cropping systems (Celik et al., 2010). During a cone penetration test, a metallic probe is inserted into the soil and the resistance to

its penetration is monitored by a load cell. The penetration resistance, expressed in megapascals (MPa), can then be obtained at high spatial resolution (down to 100 μm) in the direction of the ingression of the probe. The penetration resistance is known to be dependent on numerous edaphic factors such as soil texture (R. du T. Bennie & Burger, 1988), structure (Horn et al., 1987), water content (Lapen et al., 2004), heterogeneity, *i.e.*, the presence of soil layers having different mechanical properties (Mo et al., 2015), bulk density (Henderson et al., 1988) and the presence of roots through reinforcement (Schwarz et al., 2015).

X-ray computed tomography (CT) (Table 1) is a non-destructive scanning method which allows to visualize the three dimensional structure of opaque objects. The resulting images of X-ray CT scans are grayscale data, in which the gray value (GV) intensity is directly related to the density and the attenuation coefficient of the material which constitutes the sample (Withers et al., 2021). In a typical X-ray CT image of a soil sample, air-filled pores appear dark (*i.e.*, have a low GV) whereas denser features such as soil clods or sand grains appear brighter (*i.e.*, have a high GV). For the analysis of soil structure, most studies relying on X-ray CT put an emphasis on the pore space (after image segmentation) in order to characterize properties such as pore sizes, pore connectivity, constrictivity and bottlenecks (Weller et al., 2022; Kaur et al., 2023; Prifling et al., 2023). When focusing on the soil matrix, soil strength, as an attribute of soil structure must be in part reflected in GVs. This also makes X-ray CT a potential tool to measure local soil strength or density. So far however, only few authors have actually harnessed the underlying information contained in the grayscale data of the soil matrix as a proxy for soil density or strength (Anderson et al., 1988; Rogasik et al., 2014; Lucas et al., 2019; Phalempin et al., 2021).

X-ray CT scanning and cone penetration tests provide information which can be regarded as complimentary. Indeed, X-ray CT allows visualizing the distribution of soil deformation around the penetrometer tip. Therefore X-ray CT can provide insights into the mechanisms that are responsible for the probe resistance data. Consequently, some authors have already used X-ray CT and cone penetration tests in conjunction in order to understand the mechanical processes occurring at the tip of a penetrometer at the microscale. With the use of digital image correlation methods, Paniagua et al. (2013) were able to identify the presence of a contracting bulb of silt close to the tip of the probe surrounded by a larger bulb of dilating material. With a slightly different approach, Ngan-Tillard et al. (2005) could visualize the local deformation patterns around the penetrometer tip and showed that a dilating zone having the shape of a sphere was formed ahead of the tip. Their method relied on calibration curves which were used to convert the X-ray attenuation coefficient (expressed in Hounsfield units) to the bulk density at which the investigated sand was packed.

Both X-ray CT and cone penetration tests are recognized to be useful tools for the assessment of soil structure and its dynamics. With X-ray CT, the gray values are directly related to the local density of the scanned features. With cone penetration tests, the penetration resistance values are also directly related to the local density of the probed volume of soil around the penetrometer tip. To the best of our knowledge there are no studies which attempted to link both methods, *i.e.*, to investigate how well penetration resistance and gray values are correlated. We aimed at bridging that gap and carried out a combined analysis of the relationship PR $\sim$ GV for a large dataset of undisturbed soil cores with two soil textures, *i.e*, loam and sand.

We see a great potential in best describing the relationship PR $\sim$ GV. This would allow transforming GV data into 3D PR maps. Currently, most studies focusing on the interactions between root growth and soil physical properties usually assume these soil properties to be "bulk properties" and disregard discontinuities and microscale heterogeneity. So far, soil physical properties with respect to root growth has mostly been addressed as a bulk (Ehlers et al., 1983; Passioura, 2002; Bengough et al., 2011) or artificially, *e.g.*, with the creation of artificial macropores

(Nakamoto, 1997; Hirth et al., 2005; Colombi et al., 2017). Structured soils, however, consist of a multitude of loose and dense soil particles, of which their complex arrangements create paths of least resistance for root growth. To address the heterogeneity of soil strength at the microscale, 3D penetration resistance maps would be excellent tools. These maps would allow visualizing and analyzing the soil physical conditions in the vicinity of the roots. This would provide important knowledge on the impact of local soil strength on root-soil interactions. In this work, we provide a proof-of-concept on how to generate 3D penetration resistance maps. We also draw conclusions based on the lessons learned in that process and lay some perspectives on how such data could be used in the future.

2. Material and methods

2.1. Soil sampling

Soil sampling was carried out on a field trial located in Bad Lauchstädt, Germany (51°22′0 N, 11°49′60 E). The field trial aims at investigating the influence of root hairs and soil texture on the growth of *Zea mays* L. plants. For more information, the reader is referred to Vetterlein et al. (2021). In short, 24 rectangular plots of 34 m^2 were excavated to 1 m depth to remove the native soil and were refilled with sieved loam (12 plots) or with sand (12 plots). The substrate loam was obtained from the upper 50 cm of a haplic Phaeozem soil profile. The substrate sand constitutes of a mix of 83 % quartz sand (WF 33, Quarzwerke Weferlingen, Germany) and 17 % of the loam. Details on chemical and physical properties are provided by Vetterlein et al. (2021). The loam was sieved using a heavy duty double deck vibrating screen having a mesh aperture of 20 mm. After sieving, the loam was gradually placed in layers of 15 cm by a wheel loader, evened out with a wheel loader bucket and compacted with a vibrating plate (weight 70 kg with a pressure of 8 N cm^{-2} at reduced speed). For the sand plots, a similar procedure was employed but no vibrating plate was used. The plots were packed to a bulk density (BD) of 1.36 g cm^{-3} and 1.5 g cm^{-3} for loam and sand, respectively.

Undisturbed soil cores were extracted at the depth intervals 2.5–7.5, 12.5–17.5, 22.5–27.5 and 32.5–37.5 cm in the same pit between the rows of plants. The cores consisted of aluminum cylinders of 5 cm in height and diameter, with a wall thickness of 2 mm. To extract one core, the empty aluminum cylinder was placed in a metal casing having a slightly larger diameter than the cylinder itself and sharpened edges at the bottom. The metal casing was then carefully hammered into the soil until the cylinder was full of undisturbed soil. The core was then removed from the metal casing and cleaned of excess roots or soil at the bottom and top. After sampling, all cores were stored at 4 °C in sealed plastic bags in order to avoid desiccation prior to CT scanning. In total, 96 cores were extracted, *i.e.*, 48 for the loam, and 48 for the sand. The field trial started in March 2019 and the core sampling took place in the beginning of July of the year 2022, *i.e.*, after four year after repacking the field plots and subsequent maize cropping.

2.2. X-ray CT scanning

Directly after sampling, the samples were brought to the laboratory and X-ray CT scanning was performed with an industrial scanner (X-TEK XTH 225, Nikon Metrology) equipped with a PerkinElmer 1620 detector panel (1750 $\times$ 2000 pixels). The scanner was operated at 140 kV and 200 µA. In total, 2400 projections were acquired during the full rotation of a sample, with an exposure time of 500 ms per projection. The obtained images were reconstructed into a 3D tomogram having an 8-bit grayscale via a filtered back projection algorithm with the CT Pro 3D software (Nikon metrology). The conversion from 16-bit to 8-bit allowed saving considerable storage space without losing considerable information. During that conversion, the grayscale range was normalized with a percentile stretching method. This method sets the darkest and

Table 1
Values of the fitted parameters obtained for the loam and sand.

Parameter	Unit	Loam	Sand
V_{min}	mm^3	13.5	2.1
V_{max}	mm^3	685.4	101.6
dev_{min}	–	0.95	0.95
dev_{max}	–	1.25	1.25
str	mm	2	1
tlf	–	0.5	0.75

brightest 0.5 % voxels to 0 and 255, respectively, and performs a linear stretching in between. The images had an isotropic voxel length of 25 μm.

2.3. Micro cone penetration tests

After X-ray CT scanning penetration resistance was measured using a stainless-steel non-recessed penetration tip with a diameter of 1 mm, a length of 1.9 mm and a semi-angle of 15°. The geometry and size of the penetrometer tip were chosen so as to approximate the geometry of a root. In that way the penetration resistance would be as close as possible to the penetration resistance that roots undergo when growing in soil. This set-up is usually referred to as "micro cone penetration tests". It diverges from the typical set-ups which are commonly used in the field (Kuhwald et al., 2020; Esmailzade et al., 2022).

To perform the measurement, the shaft was connected to a material testing machine (Allround Table Top Zwick/Roell, Ulm, Germany), equipped with a sensitive force sensor with a nominal force of 100 N (accuracy grade 1 according to ISO 7500-1 down to 0.2 N at the applied load). Displacement and force were logged at every 0.1 mm depth interval. The tip was inserted from the soil surface to a depth of 39 mm into the core at a constant speed of 4 mm min^{-1}. The shaft friction was measured and corrected for by pulling out the tip at the insertion speed. The resulting forces were divided by the cross-sectional area of the shaft to provide PR values at the penetrometer tip. More details on the technical set up of the cone penetration test and the calculation of mechanical properties can be found in Rosskopf et al. (2022). Because we suspected little differences in soil matric potential, the cone penetration tests were carried out at field moist conditions.

It is worth noting that an increase of PR as a function of the depth of insertion of the penetrometer tip was observed. This behavior was ascribed to an effect of confinement pressure or to the fact that the friction along the shaft could not be completely corrected for (Mulqueen et al., 1977; Barone & Faugno, 1996; Bengough et al., 1997). In order to get rid of this artefact, the original PR dataset was filtered. The procedure carried out to filter the original PR data and some of its effects are described in the supplementary material (SM1). This increasing trend of PR with depth was not observed for the sand. Therefore the sand dataset was used without this depth correction.

2.4. Bulk soil properties

After the completion of X-ray CT scanning and PR measurements, the cores were oven-dried at 105 °C to determine bulk properties such as gravimetric water content (GWC) and BD. As bulk soil properties, we also considered the bulk PR and the bulk GV, which were obtained by averaging the depth profile of PR and GV, respectively. For the bulk GV, a circular region having a diameter of 2 mm was centered on the middle of the image and the voxels present in that region were used to calculate the average GV of that image. To characterize the degree of soil heterogeneity as another bulk soil property, we considered the coefficient of variation metric which was determined on the GV depth profile.

Because some samples were rescanned after the cone penetration tests and other samples were damaged during transport or handling, the total amount of samples considered in the analysis of the correlation between bulk soil properties was 34 and 40, for loam and sand, respectively.

2.5. Preprocessing of X-ray CT images

In order to make the gray value measurements comparable between the soil cores of a given soil texture, a set of preprocessing operations were applied on the original grayscale data. These operations entailed a histogram peak normalization and a gray value radial and vertical drift correction. The histogram peak normalization ensured that no differences in contrast were present throughout the datasets. Differences in

contrast may occur as a result of the percentile stretching method used during the conversion to 8-bit. The purpose of the gray value radial drift correction was to normalize the gray values across radial distances from the centre to the periphery of a core. This radial drift is a result of beam hardening artefacts (also known as "cupping artefact") which is typical in X-ray radiography. The gray value vertical drift correction aimed at normalizing gray values across vertical distances from the top to the bottom part of the sample. Differences in gray values in the vertical direction are known artefacts arising from the use of a conical X-ray beam, which is particular to the scanner used in this study. All image processing steps as well gray values measurements were carried out with the Fiji bundle of the free image analysis software ImageJ (Schindelin et al., 2012) and self-written macros in the ImageJ language.

2.6. Model for the zone of influence of the penetrometer tip

During the ingression of a penetrometer tip into the soil, the tip is known to have a zone of influence (ZOI) in which soil deformation occurs. The extent and size of this zone of influence depend on the local heterogeneity of the soil which the tip encounters. Indeed, the zone of influence is expected to be larger in dense soil as compared to in loose soil (Mo et al., 2015). This can be explained by the fact that in loose soil the deformation needed to accommodate the loss of volume caused by the penetrometer tip can occur in the large pores directly in the vicinity of the tip. In a denser soil, there is less pore space available and therefore, soil particles transfer the stress towards a larger volume to accommodate the deformation generated by the penetrating tip. To take such behavior into account, a new approach had to be developed to extract meaningful gray value data.

In this new approach, we considered that the volume of the ZOI (V_{ZOI}) is linearly proportional to the relative density of the soil with respect to the average gray value of a given soil texture. Mathematically, we write

$$dev_d = \frac{GV_{sw,d}}{GV_{mean}} \tag{1}$$

where dev_d is the relative soil density at depth d, $GV_{sw,d}$ is the gray value measured within a search window located at the depth d and GV_{mean} is the average gray value of a given soil texture. Practically, the ratio dev was calculated within a search window of which the extent in the vertical direction was equal to the sum of the penetrometer tip length and a parameter we coined the "stretch", also noted str (Fig. 1a). The stretch represents the vertical extent of the search window ahead of the tip. It was introduced to account for the fact that a tip can "sense" the soil strength at some distances ahead of its position (Vreugdenhil et al., 1994; Yost et al., 2022). For our analysis, we considered the search window to be a cylinder of which the diameter was equal to str and the center was aligned on the axis of the shaft of the penetrometer. The search window consists of a constant volume which moves incrementally in depth. It enables the assessment of the relative soil density, which is further used to calculate the volume of the ZOI.

Once dev was calculated for each depth increment, it could then be used to calculate V_{ZOI} according to the following model,

$$V_{ZOI,d} = V_{min} \qquad for \qquad dev_d \leq dev_{min} \tag{2}$$

$$V_{ZOI,d} = \frac{V_{max} - V_{min}}{dev_{max} - dev_{min}} dev_d + b \qquad for \qquad dev_{min} < dev_d < dev_{max} \tag{3}$$

$$V_{ZOI,d} = V_{max} \qquad for \qquad dev_d \geq dev_{max} \tag{4}$$

where $V_{ZOI,d}$ is the volume of the zone of influence of the penetrometer tip at the depth d, V_{min} and V_{max} are the minimum and maximum allowed volume of the ZOI, dev_{min} and dev_{max} are the minimum and maximum allowed deviation of GV relative to the average GV of a given soil texture, and b is the intercept, which is determined graphically (Fig. 1b). While V_{min} and V_{max} are parameters having a physical
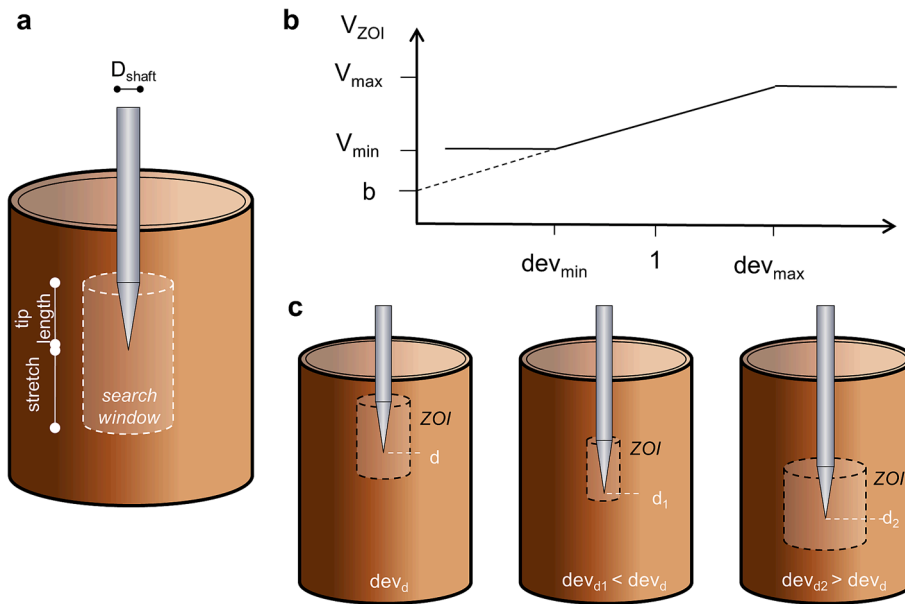
Fig. 1. Conceptual model to relate the size of the zone of influence (ZOI) of a penetrometer tip to the local soil density around the tip. (**a**) The search window is used to calculate the variable dev, which describes how much looser or denser is the zone around and ahead of the tip, in comparison to the average density of the soil. The search window has a vertical extent equal to the sum of the penetrometer tip length multiplied by the tip length factor (tlf) and a parameter we coined the "stretch" (str). (**b**) The volume of the zone of influence (V_{ZOI}) around the penetrometer tip was calculated as a linear function of dev values and bounded by the user-defined parameters V_{min}, V_{max}, dev_{min} and dev_{max}. (**c**) This approach suggests that when the penetrometer tip encounters a zone which has a higher or a lower GV than the average GV of a given soil, the size of the ZOI increases or decreases accordingly.

meaning, dev_{min} and dev_{max} are tunable parameters which govern the rate of volume change of the ZOI as a function of soil density. Here we considered the ZOI to be a cylinder with a diameter equal to its height and of which the center was aligned on the axis of the shaft of the penetrometer.

This new approach suggests that when the penetrometer tip encounters a zone which has a higher GV than the average GV of a given soil (*i.e.*, a dense zone), the size of the cylinder considered for the GV measurement around the tip increases. When the penetrometer tip encounters a zone which has a lower GV than the average GV of a given soil (*i.e.*, a loose zone), the size of the cylinder considered for the GV measurement around the tip decreases (Fig. 1c).

2.7. Model fitting

The model to calculate V_{ZOI} comprised parameters which could be easily measured or constrained. For instance, we set the constraint that the diameter of the ZOI could not be inferior to the diameter of the shaft (*i.e.*, D_{shaft}, see Fig. 1a). The average GV of a given soil texture GV_{mean} could easily be measured based on the preprocessed grayscale data. The parameters of the model were fitted iteratively and manually in order to obtain the best match possible between PR and GV for some selected samples (two to three samples per soil texture). The samples selected for the fitting were the ones which presented salient features such as a big dense loam clod located in an otherwise homogeneous and loose soil matrix. Such salient features generated peaks and valleys in the PR and GV depth profile. These features were ideal to assess visually the quality of the fit. During the fitting procedure, it was noticed that the best fits were obtained when the penetrometer tip length was allowed to be tuned. We therefore added an extra parameter, the tip length factor (noted *tlf*), which was constrained so that $0 \leq tlf \leq 1$ and which modulated the tip length by a simple multiplication. Note that in contrast to *str* which determines how far the search window extends ahead of the penetrometer tip, the parameter *tlf* governs how far the search window extends backward from the penetrometer tip. In total, our approach consisted of seven parameters, out of which six were

considered tunable (V_{min}, V_{max}, dev_{min}, dev_{max}, *str* and *tlf*).

2.8. Data analysis

Data analysis was carried out with R (Team, 2022) and graphical figures were generated with the R package "ggplot2" (Wickham & Chang, 2016). Differences in mean bulk properties were assessed with t-tests when the normal distribution and homogeneity of variance were confirmed. Otherwise the non-parametric ranking test of Wilcoxon was used to test differences in the median. In order to assess the goodness of the fit between PR and GV, the distance correlation metric (here noted d_{corr}) implemented in the R package "energy" (Rizzo and Szekely, 2022) was used. The distance correlation is a metric similar to the Pearson correlation coefficient but it is better suited than the latter to account for some non-linearity in the relationship between two variables (Székely et al., 2007) (see also the supplementary material SM2). The d_{corr} can take values between 0 and 1, with 0 meaning absolutely no correlation and 1 meaning a perfect correlation between the two considered variables.

3. Results

In loam, the bulk PR ranged from 0.67 to 15 MPa whereas it ranged from 0.3 to 4.6 MPa in sand (Fig. 2a). The difference between loam and sand was highly statistically significant (p-value < 0.001). The gravimetric water content of the samples had no impact on the bulk PR measurements (Fig. 2b). It was very different between loam and sand (p-value < 0.001, Fig. 2c). As could be expected, there was a significant correlation between bulk PR and BD (Fig. 2d) and this correlation was much stronger in loam (p-value < 0.001) than in sand (p-value < 0.05). The GWC also had no impact on the BD measurements (Fig. 2e). The BD in loam ranged from 1.22 to 1.77 g cm^{-3} whereas it ranged from 1.33 to 1.51 g cm^{-3} in sand (Fig. 2f). There was a positive and significant correlation (p-value < 0.001) between bulk PR and bulk GV in loam (Fig. 2g), however the coefficient of determination was relatively low ($R^2 = 0.32$). This correlation was absent in sand (p-value = 0.22). Here again, the wide scatter of points between bulk GV and GWC suggests that
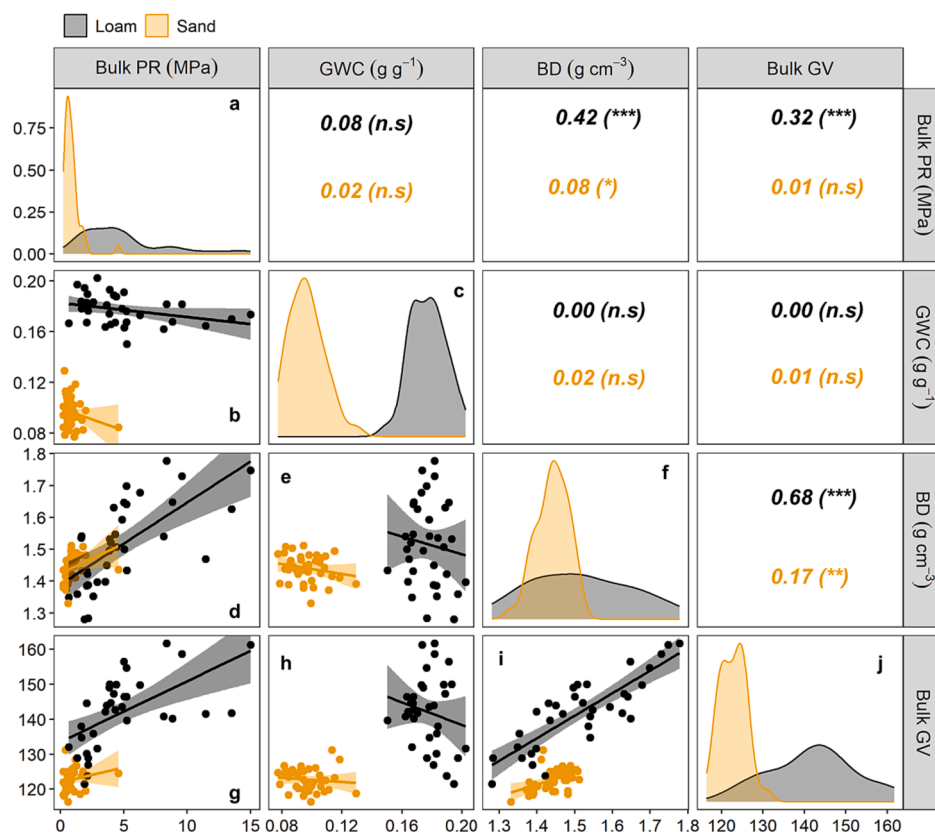
Fig. 2. Pairs of correlation between the bulk penetration resistance (bulk PR), the gravimetric water content (GWC), the bulk density (BD) and the bulk gray value (bulk GV) for samples extracted in loam (n = 34) and in sand (n = 40). The scatterplots, associated regressions lines and confidence intervals (at P = 0.95) are shown in the lower left part of the figure. The plots aligned on the diagonal axis of the figure show the density distribution of each variable. The coefficient of determination as well as the level of significance of each correlation are shown in parentheses in the upper right part (n.s = p-value > 0.05; "*"=p-value < 0.05, "**" p-value < 0.01, "***"=p-value < 0.001).

the gravimetric water content of the samples did not affect the GV measurements (Fig. 2h). The strongest correlations were found between BD and bulk GV (Fig. 2i) both in loam (p-value < 0.001) and sand p-value < 0.01. For this correlation, the highest coefficients of

determination were also observed (R^2 = 0.69 in loam and R^2 = 0.17 in sand). For loam, bulk GV ranged from 121 to 161 whereas it ranged from 116 to 131 in sand. The median of the distribution in loam was higher than in sand (p-value < 0.001) (Fig. 2j). Because of the homogeneous
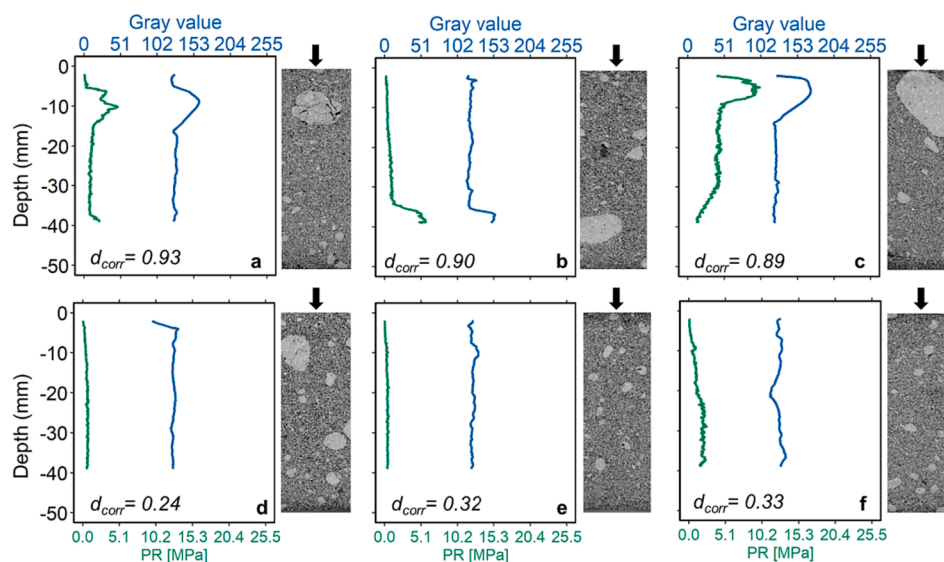

Fig. 3. Visual appreciation of the match between the PR (in green) and the GV measurements (in blue) for a selected set of sand samples. The subfigures **a,b,c** correspond to the samples having the highest d_{corr} values whereas the subfigures **d,e,f** correspond to the samples having the lowest d_{corr} values of the sand dataset. The point of insertion of the penetrometer tip into the sample is shown with a black arrow. (For interpretation of the references to colour in this figure legend, the reader is referred to the web version of this article.)

packing of the field plots, the depth at which the cores were extracted had no impact of the bulk PR (p-value > 0.16) (data not shown).

The calibration of the model to calculate the volume of the ZOI was straight forward. It took only a few iterations to find the best combination of parameters (11 and 18 iterations for sand and loam, respectively). The values of the optimized parameters are shown in Table 1.

With the optimized set of parameters, the GV measurements were carried out and the results were confronted with PR values and vertical XZ cross sections of the X-ray CT images. Some of the samples with the highest (subfigures a, b and c) and lowest d_{corr} values (subfigures d, e and f) are shown for sand (Fig. 3) and loam (Fig. 4).

For sand, d_{corr} ranged from 0.24 to 0.93. The fits with the highest d_{corr} were usually obtained for samples which had loam clods located in an otherwise homogeneous sand matrix (Fig. 3a,b,c). Because the loam clods induced a greater PR than the sand grains (Fig. 2a), PR tended to increase when the penetrometer tip encountered loam clods on its course. In that case, the peaks and valleys of PR values attributed to the presence of loam clods could generally be well captured and this contributed to an increase of d_{corr}. On the contrary, the fits with the lowest d_{corr} in sand were obtained for samples which had a homogeneous sand matrix and when the penetrometer tip did not encounter loam clods on its course (Fig. 3d,e,f). When the sand was homogeneous, the agreement was also very good, but the correlation became afflicted by random noise and by the narrow scatter of points in the 2D space of PR against GV. Both aspects contributed to a decrease in d_{corr} values.

For loam, d_{corr} ranged from 0.32 to 0.91. The fits with the highest d_{corr} values were often (but not exclusively) obtained for the samples which had dense loam clods located in an otherwise rather loose loam matrix (Fig. 4a,b,c). The fits with the lowest d_{corr} values (Fig. 4d,e,f) were usually obtained for the samples which had a dense loam matrix such as the sample shown at the Fig. 4d. In that case, the GV data showed an almost flat line which had no or very little agreement with the fluctuating PR values. To get an idea of the goodness of the match for the whole dataset, the Figures S3 and S4 in the supplementary material SM3 show plots of PR and GV for loam (n = 41) and sand (n = 46), respectively, and for each sample individually.

Based on the observations made on Figs. 3 and 4, there seems to be a relationship between d_{corr} and the soil heterogeneity. To understand the nature of this relationship, the d_{corr} values were paired with the coefficient of variation of GV, which we used as a metric for soil heterogeneity. For sand, there was a positive correlation between d_{corr} and the coefficient of variation of GV (p-value < 0.01) whereas this correlation was absent for loam (p-value = 0.69). The soil heterogeneity was much higher in loam than in sand, as the coefficient of variation of GV ranged from 3.2 to 37.6 in loam (Fig. 5a) against 6.3 to 22.8 in sand (Fig. 5b). When looking at the distribution of d_{corr} for each soil texture and for all samples individually (Fig. 5c), we observed that d_{corr} tended to be on average slightly higher in loam (d_{corr} = 0.62), as compared to in sand (d_{corr} = 0.55).

For the whole dataset, the GV and PR measurements at the microscale yielded a total of 15,200 and 17,066 pairs of points for loam (Fig. 6a) and sand (Fig. 6b), respectively. When considering all PR ~ GV pairs of points, the d_{corr} amounted to 0.66 and 0.34, for loam and sand respectively. Interestingly, computing d_{corr} for each pair of points of PR and GV at the microscale instead of core averages caused the correlation to increase from 0.62 to 0.66 in loam. In sand, the correlation collapsed from 0.55 to 0.34. For loam, the scatterplot of PR ~ GV has a shape that is reminiscent of a hyperbola, with an asymptotic GV at approximately 172. For sand, no particular model could be recognized.

Notwithstanding the great scatter but bearing in mind the original aim of this study, we continued the exercise so as to provide a proof-of-concept on how to generate PR maps with GV data. For loam, we fit a hyperbola which bests describes the relationship PR ~ GV. The hyperbola had the following form,

$$PR = \left(\frac{a}{GV_{max} - GV}\right)^b - c \qquad (5)$$

where *PR* is the predicted PR value, GV_{max} is the highest GV observed in the loam dataset, GV is the gray value to be used for the PR prediction and a, b, c are fitting parameters. The parameter c was constrained so as to avoid negative PR values for GV = 0. Because the parameters of the hyperbolic model were too correlated with each other, fit attempts with the Levenberg-Marquardt algorithm failed. The fit was therefore made manually and showed a good agreement with the experimental data (Figure S5). The fitting yielded $a = 150; b = 0.9; c = 0.88$. With this hyperbolic model, the GV data could be converted to PR (Fig. 7). Before doing so, the images were downscaled by a factor of 40, *i.e.*, each voxel has a side length of 1 mm in all directions (Fig. 7b). This was done so as to reflect the fact that the PR ~ GV relationship on which the model is based was acquired with a penetrometer tip having a diameter of 1 mm.
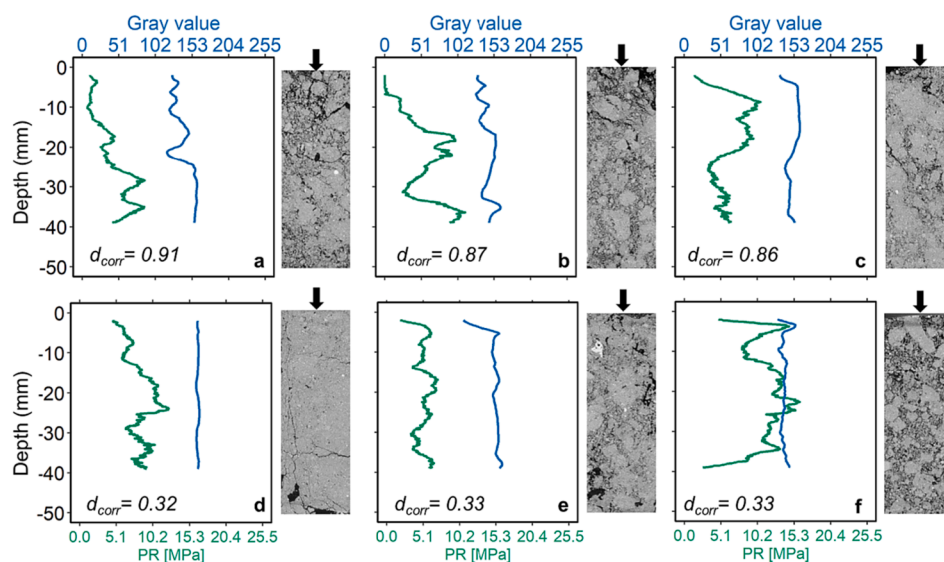

Fig. 4. Visual appreciation of the match between the PR (in green) and the GV measurements (in blue) for a selected set of loam samples. The subfigures **a,b,c** correspond to the samples having the highest d_{corr} values whereas the subfigures **d,e,f** correspond to the samples having the lowest d_{corr} values of the loam dataset. The point of insertion of the penetrometer tip into the sample is shown with a black arrow. (For interpretation of the references to colour in this figure legend, the reader is referred to the web version of this article.)
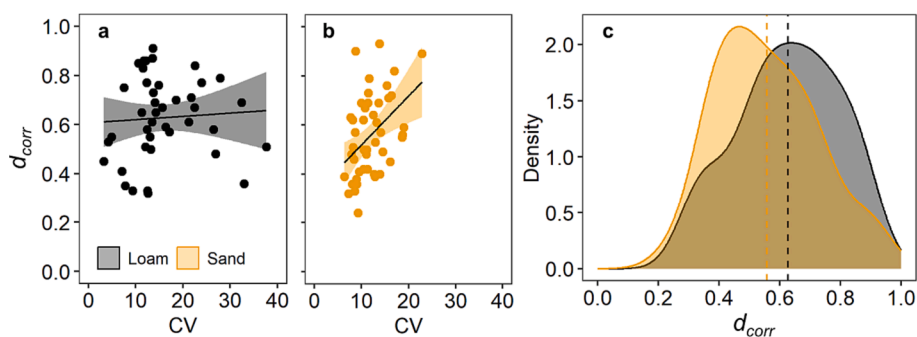
Fig. 5. Analysis of the relationship between the distance correlation metric (d_{corr}) and the soil heterogeneity as well as the d_{corr} density distribution for loam (n = 41) and sand (n = 46). (**a**) Relationship between d_{corr} and the soil heterogeneity (as assessed with the coefficient of variation of GV, noted CV) for loam. (**b**) Relationship between d_{corr} and CV for sand. (**c**) Density distribution of d_{corr} for loam and sand. The vertical dashed lines indicate the mean value of the distribution. The legend shown in subfigure **a** is valid for all other subfigures.
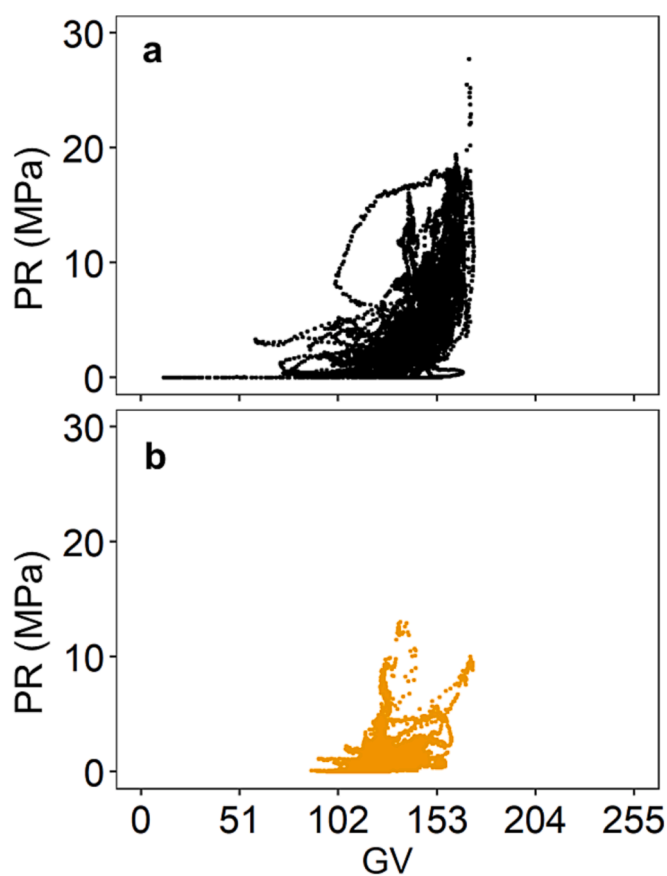

Fig. 6. Scatterplots of penetration resistance (PR) against gray value (GV) for loam (subfigure **a**; n = 15200) and for sand (subfigure **b**; n = 17066).

This limits the spatial resolution of the penetration resistance map to that length. Because the hyperbolic model only has a meaningful solution within the range $0 < GV < 172$, the voxels with $GV > 172$ were assigned to $PR \geq 30$ MPa. The voxels with $GV = 0$ were set to $PR = 0$. Possibly, some of these voxels with $GV > 172$ correspond to rigid particles much larger than the penetrometer tip (*i.e.*, small stones or concretions) for which the PR can virtually take infinite values. Because no known model could be identified on the PR ~ GV relationship for sand, we did not carry out the exercise of converting GV into PR for that soil texture.

4. Discussions

4.1. Correlations between bulk soil properties

In our study, several bulk soil properties showed positive correlations, for instance bulk PR and BD. This positive correlation is well documented in the literature, even though different models to describe it have been proposed (Vazquez et al., 1991; Grant & Lafond, 1993; Celik et al., 2010). Some authors suggest that the relationship between PR and BD is best described by a power or an exponential law (Vaz et al., 2011). With our data having a quite wide scatter of points (Fig. 2d), discerning a model that would best fit the data was not trivial. We therefore assumed a linear relationship. The correlation between bulk PR and BD in sand was lower than in loam. This is explained by the fact that (i) the sand had a very homogeneous structure (Fig. 5b) which resulted in a very narrow range of PR (Fig. 6b) and that (ii) the only high bulk PR values were recorded when the penetrometer tip hit loam clods, which was a random and rare event.

Because the cores were sampled in plots laying only a few meters apart and having homogeneous textural properties in depth, the measured GWC remained within a narrow range, *i.e.*, the difference between the maximum and the minimum GWC was approximately 0.05 only, both for loam and for sand. As a result, we found a non-significant relationship between PR and GWC, when assuming a linear model. In the literature, such a relationship is also described by either a power law (Mielke et al., 1994) or an exponential law (Busscher, 1990). The great scatter of points between PR and GWC in addition to the narrow range of GWC did not allow the identification of a suitable model. At the core scale, the observed small differences in GWC for each texture had no impact on the bulk PR (p-value = 0.056; Fig. 2b) and bulk GV measurements (p-value = 0.29; Fig. 2h).

The bulk GV and BD were also positively correlated. This correlation is inherent to the principles of X-ray CT scanning, *i.e.*, there is a linear relationship between the density of an object and the CT derived Hounsfield unit (Petrovic et al., 1982). The CT derived Hounsfield unit is also directly linearly proportional to the calculated GVs (Reeves et al., 2012). This supports previous studies which have used GV as a proxy for BD, *e.g.*, for the study of bulk density gradients around plant roots (Lucas et al., 2019; Phalempin et al., 2021), or the CT number of the soil matrix as a proxy for BD, *e.g.*, for the study of preferential flow in undisturbed soil (Katuwal et al., 2015).

4.2. Microscale approach and adaptive volume of the ZOI

We have adopted an approach which considers the dependency between PR and GV at the microscale. This approach required the development of a model (Fig. 1) and the calibration of some parameters to estimate the size of the ZOI (table 1). The necessity of calibrating a
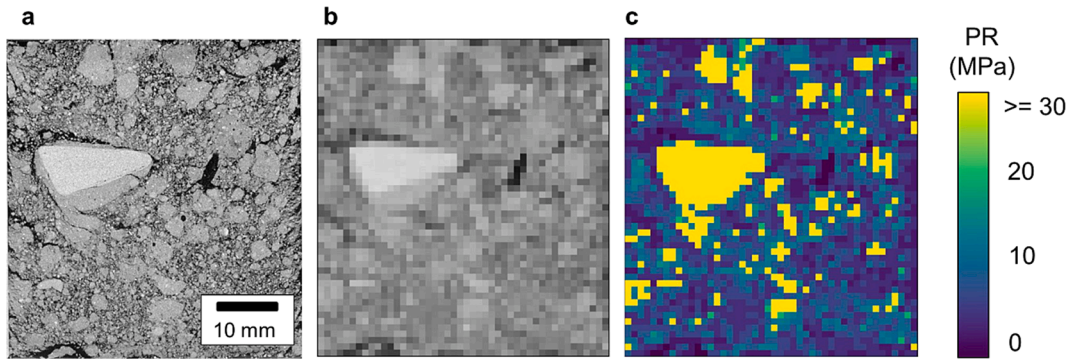
Fig. 7. Generating a penetration resistance map with gray value data. (**a**) A 2D XZ cross-section at the original resolution. (**b**) The subfigure **a** was downscaled by a factor of 40 so as to reflect the fact that the PR ~ GV relationship on which the model is based on was acquired with a penetrometer tip having a diameter of 1 mm. This limits the spatial resolution of the PR map to that length. (**c**) The penetration resistance map. The scale bar of subfigure **a** is also valid for the subfigure **b** and **c**.

model prior to the GV measurements can be considered a drawback in comparison to a bulk approach. With a bulk approach the GV and PR values are simply averaged over depth for each sample and compared with no consideration for microscale heterogeneity (see Fig. 2g). The benefit of the microscale approach is that it allowed generating a high number of data points of PR and GV. These numerous data points further enabled the identification of the hyperbolic model for the loam dataset. In contrast, building a reliable model based on a bulk approach would require sampling and measuring many more soil cores which is usually time-consuming and laborious.

To carry out the GV measurements at the microscale, we considered an adaptive volume of the zone of influence of the penetrometer tip as a function of soil density. We did so because the deformation zone and hence the volume in which we can expect changes in GV depends on the local structure. Therefore, it cannot be considered constant along the trajectory of the penetrometer tip. Note that if we had considered a constant V_{ZOI} value (corresponding to the median of the distribution of V_{ZOI} values used for the GV measurements), the distance correlation would have reached 0.47 and 0.22 only, for loam and sand, respectively. These numbers illustrate well the benefits of considering an adaptive volume of the ZOI, in comparison to a constant volume.

4.3. Estimation of the zone of influence of the penetrometer tip

Knowing the geometry of the cylindrical ZOI and taking into account the tip length, we can convert volume into diameter and express these values in terms of a ratio of the diameter of the ZOI (D_{ZOI}) over the diameter of the shaft (D_{shaft}). This allows an easier comparison with the literature data regarding the size and geometry of the ZOI. By doing so, we found that D_{ZOI}/D_{shaft} ranged from 1 to 4.62 for sand, with a median value of 2.15 (Fig. 8). In Paniagua et al. (2013), the extent of the ZOI was aproximately three times the diameter of the shaft horizontally and vertically. Ngan-Tillard et al. (2005) reported that the loosening zone in direct contact with the cone tip had an external diameter of up to 2.6 times the cone diameter. They have tested a uniform sand with a mean grain diameter of 150 μm, which is similar to the fine sand matrix of the sand mixture of our study (median grain diameter of 160 μm; see also Fig. 6b in Phalempin et al. (2021)). In Mo et al. (2015), the observable lateral influence zone was about five times the shaft diameter for dense sand, and approximately 3.5 times the shaft diameter for loose sand with a mean diameter of the sand of 140 μm. The observed values of the extent of the ZOI for sand are well in accordance with the values in the literature.

In loam, D_{ZOI}/D_{shaft} ranged from 2.3 to 9.2, with a median value of 4.3. These values are higher than in sand. They are also higher than the values found in the literature. One possible reason for this difference is that the loam had highly cohesive soil clods. These cohesive soil clods acted as large soil particles, which were bigger than the sand grains.
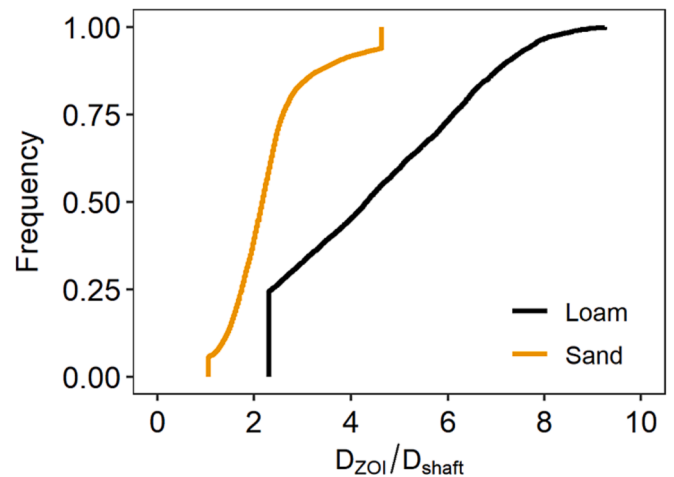

Fig. 8. Frequency distribution of the ratio of the diameter of the cylindrical zone of influence of the penetrometer tip (D_{ZOI}) over the diameter of the shaft (D_{shaft}) which were used for the measurements of gray value.

Possibly, the volume of ZOI concomitantly increases with particle size because the bigger the soil particles, the greater the zone of the soil affected by their moving and tilting, as the penetrometer tip hits them. Note that, because our reported D_{ZOI}/D_{shaft} values are based on fitting parameters of a model, an experimental validation of the extent of the zone in which particles displacement occur is still necessary (*e.g.*, following the procedure of Koestel and Schlüter (2019)).

To estimate the size of the ZOI, we have included the parameters *str* and *tlf*. Both parameters were useful to tune the GV measurements such that the peaks and valleys of GV and PR aligned. We have also included the parameters dev_{min} and dev_{max} which governed the rate of volume change of the ZOI with respect to the soil density. To the best of our knowledge, no other studies have integrated such parameters in their analysis; therefore no comparison is possible.

4.4. Limitations and uncertainties

On the PR ~ GV relationship for loam, we have observed a great scatter of points which affects the quality of the PR predictions. This scatter of points results from several factors which added uncertainties to the PR and GV measurements. These are related to the interacting edaphic factors influencing soil strength, to the exact position of the penetrometer tip, to the shape of the ZOI and to the effect of confining pressure and shaft friction.

Soil strength is a complex soil property which depends on numerous edaphic interacting factors (Bengough et al., 2011). It is not only

induced by the arrangement of individual soil particles, but it is also influenced by the cohesion and structural bonds caused by cements or gluing agents (Rosskopf et al., 2022). It is also influenced by the soil water menisci forces (Dexter et al., 2007; Bengough et al., 2011) and the number of contact points between soil particles, which in turn defines how the frictional stress is transferred from one particle to another (Peth et al., 2010). Despite the fact that grayscale data contain to some extent the information of the arrangement of soil particles and the density of objects, the apparent cohesion, structural bonds and interacting factors cannot be seen or measured with an industrial X-ray CT scanner. This added some uncertainties regarding their contribution to the PR and GV measurements at the microscale.

An uncertainty related to the GV measurements is the exact position of the penetrometer tip over its course into the sample. Rescanning a few samples with X-ray CT after the cone penetration tests, we observed a tendency of the shaft to bend or to be deflected by rigid features. Based on these second scans, we calculated an average offset in the $\times$ and y-direction of 1.1 mm (standard error = 0.24) in loam (n = 7). In sand (n = 2), we observed an average offset of 0.81 mm (standard error = 0.30) in the x-direction and 1.13 mm in y-direction (standard error = 0.25). Because we considered that the center of the ZOI was aligned on the axis of the shaft of the penetrometer, any offset in the shaft position introduces a certain bias in the GV measurements and therefore affects the scatter of points on the PR ∼ GV relationship.

Another uncertainty in the GV measurements is related to the shape of the ZOI. Typically, the penetration of a tip into the soil leads to a cylindrical deformation zone around the probe shaft and a spherical deformation region ahead of the tip (Mo et al., 2017). In our study, we considered a cylindrical shape of the ZOI (Fig. 1) because of the limitations of the image processing software we used. This potentially creates a deviation from the physical reality associated to the volume of influence of a penetrometer tip.

Finally, another factor which contributed to the scatter of points is the effect of confinement pressure or to the fact that the friction along the shaft could not be completely corrected for. This occasionally caused an increase in PR values, for no apparent counter increase in GV. Despite the fact that removing partially these effects by manipulating the PR dataset had a positive influence on the correlation between GV and PR (Fig. S2), it was not always fully successful. Indeed, a small PR increase in depth was still discernable for some samples (Figs. 4b and 4d). Note that the friction along the shaft was also probably increased when the shaft bended on the penetrometer course. Such effect is difficult to account and correct for.

5. Conclusion

The answer to the question posed in the title of the manuscript is yes, we can use X-ray CT to generate 3D penetration resistance maps. We have presented in this manuscript a proof-of-concept on how to proceed. However, when attempting to convert GV to PR data, one has to keep in mind that the PR ∼ GV relationship derived in this work cannot be applied to any soil sample. Indeed, independent penetration resistance measurements have to be conducted alongside X-ray CT in order to build a reliable PR ∼ GV model. The success of building a reliable model depends on numerous factors related to soil properties such as soil texture, structure or matric potential. It also depends on technical modalities related to the X-ray CT scanning. Such technical modalities include for instance the choice of appropriate percentage values for the percentile stretching method, which in turn determines the contrast of the images. Another limitation of the presented approach is the final spatial resolution resulting from the data merging of X-ray CT scanning and cone penetration tests. Despite the fact that X-ray CT can achieve a spatial resolution at the micrometer scale, our approach was limited by the diameter of the shaft, which reduced the analysis to a millimeter scale resolution. Note that, in reality, the lateral resolution of a cone penetration test is equal to the radius of the ZOI.

Yet, despite the aforementioned limitations, we see a great potential in applying the presented methodology in soil science, particularly in the field of root-soil interactions research and plant breeding. With 3D penetration resistance maps at hand, it would be possible to perform comprehensive and non-invasive analysis on how roots (preferentially) grow in zones of soil having different mechanical properties. With modern agriculture facing soil compaction problems worldwide, this can be particularly relevant for the study and breeding of cultivars that could show plastic response of their root systems under mechanical stress (Correa et al., 2019).

In this study, we have investigated two soils which were fairly homogeneous. Natural soils are, however, usually more heterogeneous. The natural continuation of this work is to investigate a larger panel of soil types. This panel will include soils with more heterogeneous structure as well as larger variations in stone, water and clay contents. This will allow the establishment of numerous PR ∼ GV relationships, with the potential of finding a more general conversion model. This general conversion model should include parameters which could be derived via pedotransfer functions, *i.e.*, based on easily-measurable bulk properties of soil.

Declaration of Competing Interest

The authors declare that they have no known competing financial interests or personal relationships that could have appeared to influence the work reported in this paper.

Data availability

Data will be made available on request.

Author contributions

MP carried out the undisturbed core sampling, the X-ray CT scanning, the processing of the images and subsequent measurements of GV. MP conceptualized and implemented the model used to relate the size of ZOI to the soil density around the penetrometer tip. MP produced all figures and wrote the original draft of the manuscript. UR carried out the PR and GWC measurements. MP; UR; SS, DV and SP designed the study. SS, DV and SP are responsible for funding acquisition. All authors read, edited and approved the final manuscript.

Appendix A. Supplementary data

Supplementary data to this article can be found online at https://doi.org/10.1016/j.geoderma.2023.116700.

References

Anderson, S.H., Gantzer, C.J., Boone, J.M., Tully, R.J., 1988. Rapid Nondestructive Bulk Density and Soil-Water Content Determination by Computed Tomography. Soil Sci. Soc. Am. J. 52 (1), 35–40.

Barone, L., Faugno, S., 1996. Penetration Tests for Measurement of Soil Strength: Assessment of the Contribution of Shaft Friction. J. Agric. Eng. Res. 64 (2), 103–108.

Bauder, J., Randall, G., Swann, J., 1981. Effect of four continuous tillage systems on mechanical impedance of a clay loam soil. Soil Sci. Soc. Am. J. 45 (4), 802–806.

Bengough, A.G., Mullins, C.E., Wilson, G., 1997. Estimating soil frictional resistance to metal probes and its relevance to the penetration of soil by roots. Eur. J. Soil Sci. 48 (4), 603–612.

Bengough, A.G., McKenzie, B.M., Hallett, P.D., Valentine, T.A., 2011. Root elongation, water stress, and mechanical impedance: a review of limiting stresses and beneficial root tip traits. J. Exp. Bot. 62 (1), 59–68.

Bennie, A.T.P., Burger, R.d.T., 1988. Penetration resistance of fine sandy apedal soils as affected by relative bulk density, water content and texture. S. Afr. J. Plant Soil 5 (1), 5–10.

Busscher, W., 1990. Adjustment of flat-tipped penetrometer resistance data to a common water content. Transactions of the ASAE 33 (2), 519–0524.

Celik, I., Gunal, H., Budak, M., Akpinar, C., 2010. Effects of long-term organic and mineral fertilizers on bulk density and penetration resistance in semi-arid Mediterranean soil conditions. Geoderma 160 (2), 236–243.

Colombi, T., Braun, S., Keller, T., Walter, A., 2017. Artificial macropores attract crop roots and enhance plant productivity on compacted soils. Sci. Total Environ. 574, 1283–1293.

Correa, J., Postma, J.A., Watt, M., Wojciechowski, T., Zhang, J., 2019. Soil compaction and the architectural plasticity of root systems. J. Exp. Bot. 70 (21), 6019–6034.

Dexter, A.R., Czyż, E.A., Gaţe, O.P., 2007. A method for prediction of soil penetration resistance. Soil Tillage Res. 93 (2), 412–419.

Ehlers, W., Köpke, U., Hesse, F., Böhm, W., 1983. Penetration resistance and root growth of oats in tilled and untilled loess soil. Soil Tillage Res. 3 (3), 261–275.

Esmailzade, M., Eslami, A., Nabizadeh, A., Aflaki, E., 2022. Effect of Cone Diameter on Determination of Penetration Resistance Using a FCV. Int. J. Civil Eng. 20 (2), 223–236.

Grant, C.A., Lafond, G.P., 1993. The effects of tillage systems and crop sequences on soil bulk density and penetration resistance on a clay soil in southern Saskatchewan. Can. J. Soil Sci. 73 (2), 223–232.

Henderson, C., Levett, A., Lisle, D., 1988. The effects of soil water content and bulk density on the compactibility and soil penetration resistance of some Western Australian sandy soils. Soil Res. 26 (2), 391–400.

Hirth, J.R., McKenzie, B.M., Tisdall, J.M., 2005. Ability of seedling roots of Lolium perenne L. to penetrate soil from artificial biopores is modified by soil bulk density, biopore angle and biopore relief. Plant and Soil 272 (1), 327–336.

Horn, R., Stork, J., Dexter, A., 1987. Untersuchungen über den Einfluss des Bodengefüges für den Eindringwiderstand in Böden. Z. Pflanzenernahr. Bodenk. 150 (5), 342–347.

Katuwal, S., Moldrup, P., Lamandé, M., Tuller, M., de Jonge, L.W., 2015. Effects of CT Number Derived Matrix Density on Preferential Flow and Transport in a Macroporous Agricultural Soil. Vadose Zone J. 14 (7), 1–13.

Kaur, P., Lamba, J., Way, T.R., Sandhu, V., Balkcom, K.S., Sanz-Saez, A., Watts, D.B., 2023. Cover crop effects on X-ray computed tomography–derived soil pore characteristics. J. Soil. Sediment.

Koestel, J., Schlüter, S., 2019. Quantification of the structure evolution in a garden soil over the course of two years. Geoderma 338, 597–609.

Kuhwald, M., Hamer, W.B., Brunotte, J., Duttmann, R., 2020. Soil Penetration Resistance after One-Time Inversion Tillage: A Spatio-Temporal Analysis at the Field Scale. Land 9 (12), 482.

Lampurlanés, J., Cantero-Martínez, C., 2003. Soil bulk density and penetration resistance under different tillage and crop management systems and their relationship with barley root growth. Agron. J. 95 (3), 526–536.

Lapen, D.R., Topp, G.C., Edwards, M.E., Gregorich, E.G., Curnoe, W.E., 2004. Combination cone penetration resistance/water content instrumentation to evaluate cone penetration–water content relationships in tillage research. Soil Tillage Res. 79 (1), 51–62.

Lucas, M., Schlüter, S., Vogel, H.-J., Vetterlein, D., 2019. Roots compact the surrounding soil depending on the structures they encounter. Sci. Rep. 9 (1), 1–13.

Lunne, T., Powell, J.J., Robertson, P.K., 2002. Cone penetration testing in geotechnical practice. CRC Press.

Mielke, L.N., Powers, W.L., Badri, S., Jones, A.J., 1994. Estimating soil water content from soil strength. Soil Tillage Res. 31 (2), 199–209.

Mo, P.-Q., Marshall, A.M., Yu, H.-S., 2015. Centrifuge modelling of cone penetration tests in layered soils. Géotechnique 65 (6), 468–481.

Mo, P.-Q., Marshall, A.M., Yu, H.-S., 2017. Layered effects on soil displacement around a penetrometer. Soils Found. 57 (4), 669–678.

Mulqueen, J., Stafford, J.V., Tanner, D.W., 1977. Evaluation of penetrometers for measuring soil strength. J. Terramech. 14 (3), 137–151.

Nakamoto, T., 1997. The distribution of maize roots as influenced by artificial vertical macropores. Japan. J. Crop Sci. 66 (2), 331–332.

Ngan-Tillard, D.J.M., Cheng, X.H., Jv, N., Zitha, P.L.J., 2005. Application of X-ray Computed Tomography to Cone Penetration Tests in Sands. Site Characteriz. Model. 1–12.

Paniagua, P., Andó, E., Silva, M., Emdal, A., Nordal, S., Viggiani, G., 2013. Soil deformation around a penetrating cone in silt. Géotechnique Lett. 3 (4), 185–191.

Passioura, J.B., 2002. Soil conditions and plant growth. Plant Cell Environ. 25 (2), 311–318.

Peth, S., Nellesen, J., Fischer, G., Horn, R., 2010. Non-invasive 3D analysis of local soil deformation under mechanical and hydraulic stresses by μCT and digital image correlation. Soil Tillage Res. 111 (1), 3–18.

Petrovic, A.M., Siebert, J.E., Rieke, P.E., 1982. Soil Bulk Density Analysis in Three Dimensions by Computed Tomographic Scanning. Soil Sci. Soc. Am. J. 46 (3), 445–450.

Phalempin, M., Lippold, E., Vetterlein, D., Schlüter, S., 2021. Soil texture and structure heterogeneity predominantly governs bulk density gradients around roots. Vadose Zone J. 20 (5), e20147.

Prifling, B., Weber, M., Ray, N., Prechtel, A., Phalempin, M., Schlüter, S., Vetterlein, D., Schmidt, V., 2023. Quantifying the Impact of 3D Pore Space Morphology on Soil Gas Diffusion in Loam and Sand. Transp. Porous Media 149 (2), 501–527.

Reeves, T., Mah, P., McDavid, W., 2012. Deriving Hounsfield units using grey levels in cone beam CT: a clinical application. Dentomaxillofacial Radiology 41 (6), 500–508.

Rizzo M, and Szekely, G 2022. energy: E-Statistics: Multivariate Inference via the Energy of Data. R package version 1.7-10.

Rogasik, H., Schrader, S., Onasch, I., Kiesel, J., Gerke, H.H., 2014. Micro-scale dry bulk density variation around earthworm (Lumbricus terrestris L.) burrows based on X-ray computed tomography. Geoderma 213, 471–477.

Rosskopf, U., Uteau, D., Peth, S., 2022. Effects of mucilage concentration at different water contents on mechanical stability and elasticity in a loamy and a sandy soil. Eur. J. Soil Sci. 73 (1), e13189.

Schindelin, J., Arganda-Carreras, I., Frise, E., Kaynig, V., Longair, M., Pietzsch, T., Preibisch, S., Rueden, C., Saalfeld, S., Schmid, B., Tinevez, J.-Y., White, D.J., Hartenstein, V., Eliceiri, K., Tomancak, P., Cardona, A., 2012. Fiji: an open-source platform for biological-image analysis. Nat. Methods 9 (7), 676–682.

Schwarz, M., Rist, A., Cohen, D., Giadrossich, F., Egorov, P., Büttner, D., Stolz, M., Thormann, J.-J., 2015. Root reinforcement of soils under compression. J. Geophys. Res. Earth 120 (10), 2103–2120.

Székely, G.J., Rizzo, M.L., Bakirov, N.K., 2007. Measuring and testing dependence by correlation of distances. The Annals of Statistics 35(6), 2769–2794, 2726.

Team RC R: A language and environment for statistical computing 2022.

Vaz, C.M.P., Manieri, J.M., de Maria, I.C., Tuller, M., 2011. Modeling and correction of soil penetration resistance for varying soil water content. Geoderma 166 (1), 92–101.

Vazquez, L., Myhre, D.L., Hanlon, E.A., Gallaher, R.N., 1991. Soil penetrometer resistance and bulk density relationships after long-term no tillage. Commun. Soil Sci. Plant Anal. 22 (19–20), 2101–2117.

Vetterlein, D., Lippold, E., Schreiter, S., Phalempin, M., Fahrenkampf, T., Hochholdinger, F., Marcon, C., Tarkka, M., Oburger, E., Ahmed, M., et al., 2021. Experimental platforms for the investigation of spatiotemporal patterns in the rhizosphere—Laboratory and field scale. J. Plant Nutr. Soil Sci. 184 (1), 35–50.

Vreugdenhil, R., Davis, R., Berrill, J., 1994. Interpretation of cone penetration results in multilayered soils. Int. J. Numer. Anal. Meth. Geomech. 18 (9), 585–599.

Weller, U., Albrecht, L., Schlüter, S., Vogel, H.J., 2022. An open Soil Structure Library based on X-ray CT data. Soil 8 (2), 507–515.

Wickham, H., Chang, W., 2016. Package 'ggplot2' Create Elegant Data Visualisations Using the Grammar of Graphics. Version 2 (1), 1–189.

Withers, P.J., Bouman, C., Carmignato, S., Cnudde, V., Grimaldi, D., Hagen, C.K., Maire, E., Manley, M., Du Plessis, A., Stock, S.R., 2021. X-ray computed tomography. Nat. Rev. Methods Prim. 1 (1), 18.

Yost, K.M., Yerro, A., Green, R.A., Martin, E., Cooper, J., 2022. MPM Modeling of Cone Penetrometer Testing for Multiple Thin-Layer Effects in Complex Soil Stratigraphy. J. Geotech. Geoenviron. Eng. 148 (2), 04021189.